Elucidating the Chemical Order and Disorder in High-Entropy MXenes: A High-Throughput Survey of the Atomic Configurations in $TiVNbMoC_3$ and $TiVCrMoC_3$

Zhidong Leong[†], Hongmei Jin[†], Zicong Marvin Wong[†], Kartik Nemani[§], Babak Anasori[§], and Teck Leong Tan[†]*

[†]Institute of High Performance Computing, Agency for Science, Technology and Research, 1 Fusionopolis Way, #16-16 Connexis, Singapore

[§]Department of Mechanical and Energy Engineering, Purdue School of Engineering and Technology and Integrated Nanosystems Development Institute, Indiana University-Purdue University Indianapolis, Indianapolis, Indiana 46202, United States

ABSTRACT: Expanding the MXene design space from ordered and random double-transition-metal (DTM) MXenes to include high-entropy (HE) MXenes with four or more principal elements enables a powerful approach for enhancing MXene properties. While many DTM MXenes possess unique structures that strongly influence material properties, HE MXenes are largely unknown because they are only recently synthesized. Since certain combinations of transition metals (TMs), *e.g.*, Mo-Ti and Cr-Ti, lead to ordered DTM MXene phases, where Mo/Cr atoms occupy the outer TM layers and Ti atoms occupy the inner layers, it is critical to investigate any possibilities of TM segregation in the atomic layers of HE MXenes. Therefore, we present a high-throughput first-principles study of the atomic configurations of two recently synthesized HE M_4C_3 MXenes: $TiVNbMoC_3$ and $TiVCrMoC_3$. Combining density functional theory, cluster expansion, and Monte Carlo simulations, we predict a unique preferential occupancy of the TM atoms in the four layers within the single-phase HE MXenes, even at temperatures as high as 2900 K. Across a wide compositional range, the outer (inner) layers are predominantly occupied by two of the four TM elements, with Cr most preferentially occupying the outer layers, followed by Mo, V, Nb, and Ti. The strong compositional dependence of the interlayer segregation highlights the HE MXenes' tunability. Within each TM layer, the atoms largely form a solid solution, with a tendency for Nb-V separation at lower temperatures. Our results elucidate the chemical order and disorder in HE MXenes, guiding experiments in designing MXenes with enhanced properties within the huge compositional space.

Introduction

MXenes—a novel family of layered 2D transition metal (TM) carbides and nitrides—possess unique combinations of functional and mechanical properties that enable wide-ranging applications from electrocatalysis and energy storage[1–5] to membrane filtration[6] and to smart textiles.[7] With a chemical formula of $M_{n+1}X_nT_x$ ($n = 1–4$), MXenes consist of $n + 1$ layers of TM atoms, M, interleaved with n layers of carbon or nitrogen atoms, X, with the outermost TM layers bonded to surface terminations, T, such as –O, –OH, and –F. Due to the large design space, MXenes have huge potential for compositional tuning: by alloying different pairs of TMs together, the resulting double-transition-metal (DTM) MXenes exhibit unique structures and arrangements of atoms.[8–11] DTM MXenes can form random solid solutions (SS), *e.g.*, in $(Ti,V)_2C$ and $(Nb,V)_2C$, as well as ordered DTM MXenes, such as Mo_2TiC_2 and Cr_2TiC_2.[10] In ordered DTM MXenes, one of the two TMs occupy the outer atomic layers (Mo and Cr) while the other TM (Ti) occupy the inner atomic layer. This segregation of TM pairs in 2D materials is unique to MXenes.[12,13]

Extending the MXene design space to include high-entropy (HE) MXenes with four or more principal TM elements further enhances tunability. Consequently, the development of HE MXenes has been identified as one of the key challenges in MXene research.[14] While numerous DTM MXenes have been characterized,[3] only five HE MXenes have been synthesized so far—$TiVNbMoC_3$,[15] $TiVCrMoC_3$,[15] $(TiVZrNbTa)_2C$,[16] $(Ti\text{-}V\text{-}Zr\text{-}Nb\text{-}Ta)_2C_xN_{1-x}$,[17] and $Ti_{1.1}V_{0.7}Cr_xNb_{1.0}Ta_{0.6}C_3$[18,19]—where little is known about their structure-property correlation.

The extension from DTM MXenes to HE MXenes parallels the development of HE bulk 3D alloys (HEAs)[20,21] over the past decade and a half, as well as the realization of bulk HE carbides in 2017–2018.[22,23] The design strategy uses the increased configurational entropy in HEAs and HE carbides to stabilize the SS phase, avoiding the formation of brittle intermetallics that often plague

conventional alloys.[21] Compositional tuning within the huge design space has so far produced HE materials with properties superior to those of their constituent mono-elemental counterparts. The vast compositional space has enabled radical design paradigms inspiring applications of these HE materials towards thermal protection systems, catalysis, water splitting, and structural reinforcements.[24]

However, the vast compositional space is a double-edged sword: while allowing for superior tunability, it complicates understanding, and design principles are often elusive as HEA experiments are largely limited to a few compositions at a time. If the development of HEA were any indication, it would be challenging to understand the behavior of HE MXenes across the huge compositional design space. This challenge is further exacerbated by the fact that data for MXenes are much more limited than those for bulk metal alloys, for which thermodynamic databases (*e.g.*, CALPHAD[25,26]) and phenomenological models (*e.g.*, Miedema method[25,27]) are readily available to predict phase stability and microstructure.

Here, we present a high-throughput first-principles study of two recently synthesized[15] HE MXenes—$(Ti\text{-}V\text{-}Nb\text{-}Mo)_4C_3$ and $(Ti\text{-}V\text{-}Cr\text{-}Mo)_4C_3$—to elucidate the atomic configurations and the stability of the SS phase. Such structural information is difficult to assess precisely in experiments. Unlike bulk alloys, the lower dimensionality of 2D nanoscale structures such as MXenes promotes preferential occupancy of the TM atoms, where the interlayer and intralayer atomic arrangements could differ, while still forming in single-phase, crystalline, and solid solutions structures. As we will explain in this work, the competing effects of interlayer segregation (surface science effects) and intralayer chemical order produce structural complexities in HE MXenes that differ from typical bulk HE materials.

Using Monte Carlo simulations with effective interactions trained from first-principles calculations via the cluster expansion method,[28] we predict the complex HE MXene structures across a wide range of compositions and temperatures. In general, the HE MXenes can be described as having the outer (inner) layers predominantly occupied by two of the four TMs without any visible long-range intralayer order, with a third minority species interspersed among the two dominant species. More precisely, between 900 K and 2900 K, interlayer atomic segregation of the TMs is the predominant behavior, and the segregation increases as the temperature decreases. Consistently across the compositional space, Cr most preferentially occupies the outer atomic layers, followed by Mo, V, Nb, and Ti. Equivalently, Ti most preferentially occupies the inner layers, followed by Nb, V, Mo, and Cr. Within each layer, the various TM species largely form a random SS, with a notable (intralayer) tendency for Nb and V in the inner layers to separate from each other. We demonstrate that, due to the effects of configurational entropy, this intralayer chemical order is weaker in HE MXenes than in the DTM counterparts. Our results elucidate the structural complexities in HE MXenes, guiding experiments in designing MXenes with enhanced properties.

High-throughput methodology

To tackle the vast compositional space, we employ cluster expansion[28–30] to construct surrogate models of the MXene configurational energies. Based on a generalized Ising model, cluster expansion is a popular computational technique for studying metal alloys. Trained with a small set of first-principles energies from density functional theory (DFT), the surrogate models are parametrized by physically meaningful effective interactions, allowing rapid and accurate computations of the configurational energies for any alloy structure. This enables high-throughput Monte Carlo simulations to probe the atomic arrangements in HE MXenes across compositions

and temperatures. This approach correctly accounts for the effects of configurational entropy, which is an important advantage over previous MXene studies using only DFT calculations.[10] In our calculations we excluded the surface terminations and only focused on the four layers of TMs with a layer of carbon between each layer in the M-C-M-C-M-C-M arrangement of M_4C_3 MXene. We also omitted the presence of vacancies generated during the etching of the parent MAX phase. This is because vacancies generated at the low etching temperature (328 K[15]) would have limited diffusion and thus would not significantly alter the atomic configurations in the MXenes. The Methods section details our methodology.

Results

Equicomposition

We start by examining the two HE MXenes at equi-atomic composition. Figure 1 shows the TM occupancies of the four metal layers within the $TiVNbMoC_3$ and $TiVCrMoC_3$ across the wide temperature range of 464 K to 2900 K. Although the lower and higher ends of this temperature range might be experimentally inaccessible due to sluggish diffusion and phase instability, respectively, our results in these extreme temperature regimes provide theoretical insights into the chemical order/disorder tendencies of the transition metals in HE MXenes.

Interlayer Segregation

Between 928 K and 2900 K, the predominant behavior is atomic interlayer segregation, where two of the four TMs segregate to the surfaces, that is, the outer M layers, with increasing segregation as the temperature decreases. We quantify the degree of interlayer segregation of each species by the order parameter,

$$\alpha_{\text{out-in}} = \frac{x_M^{\text{out}} - x_M^{\text{in}}}{x_M^{\text{out}} + x_M^{\text{in}}}, \quad (1)$$

where $x_M^{\text{out(in)}}$ is the concentration of species M in the outer (inner) layers. By definition, a more positive (negative) $\alpha_{\text{out-in}}$ corresponds to a higher tendency for M atoms to occupy the outer (inner) layers. Specifically, $\alpha_{\text{out-in}} = +1\ (-1)$ corresponds to perfect interlayer segregation, where all atoms of each M elements occupy the outer (inner) layers, while $\alpha_{\text{out-in}} = 0$ implies that the four M elements equally occupy the outer and inner layers (*i.e.*, no interlayer segregation).

For $TiVNbMoC_3$, Figure 1a shows that Mo and V ($\alpha_{\text{out-in}} > 0$) prefer the outer M layers while Nb and Ti ($\alpha_{\text{out-in}} < 0$) prefer the inner M layers. As the $\alpha_{\text{out-in}}$ values indicate, Mo (Ti) has the strongest tendency to segregate to the outer (inner) layer because its $\alpha_{\text{out-in}}$ is closest to $+1\ (-1)$ among the four TMs. The segregation is significant even at temperatures as high as 2900 K and grows as the temperature decreases; hence, one would expect the segregation to persist at experiment synthesis temperatures (1873 K[15]). For $TiVCrMoC_3$ (in which Cr replaced Nb), Figure 1b shows a similar interlayer segregation. However, it is now Cr and Mo preferring the outer layers, while V and Ti prefer the inner layers; the presence of Cr forces V from the outer to the inner layers. Compared to Mo, Cr even more strongly prefers the outer layers, because Cr has a more positive $\alpha_{\text{out-in}}$ than Mo. Altogether, our results suggest that the TM's relative tendencies for occupying the outer layers are given by Cr > Mo > V > Nb > Ti.

The preferential occupancy and segregation of the TMs in the four metal layers of M_4C_3 HE MXenes agree with the slight selective etching of certain TMs (V, Cr, and Mo) during the HE MXenes synthesis.[15] While all four M elements had a similar stoichiometric ratio in the starting HE $TiVNbMoC_3$ and $TiVCrMoC_3$ MXene precursors, the Mo/V and Cr/Mo content of the as-synthesized HE MXenes were less than those of Ti/Nb and Ti/V, respectively. It is known that during the harsh selective etching conditions of MXenes synthesis in hydrofluoric acid, some of the outer TMs can be removed, leaving behind atomic and cluster vacancies.[31] We speculate that

some of the outer TMs can be partially removed during the etching of the HE MXenes, leading to the lower atomic content of those elements that occupy the outer layers. Further experimental investigations are needed to confirm the correlation of the outer layer occupancies and their lower-than-stoichiometric content in the as-synthesized HE $TiVNbMoC_3$ and $TiVCrMoC_3$ MXenes.

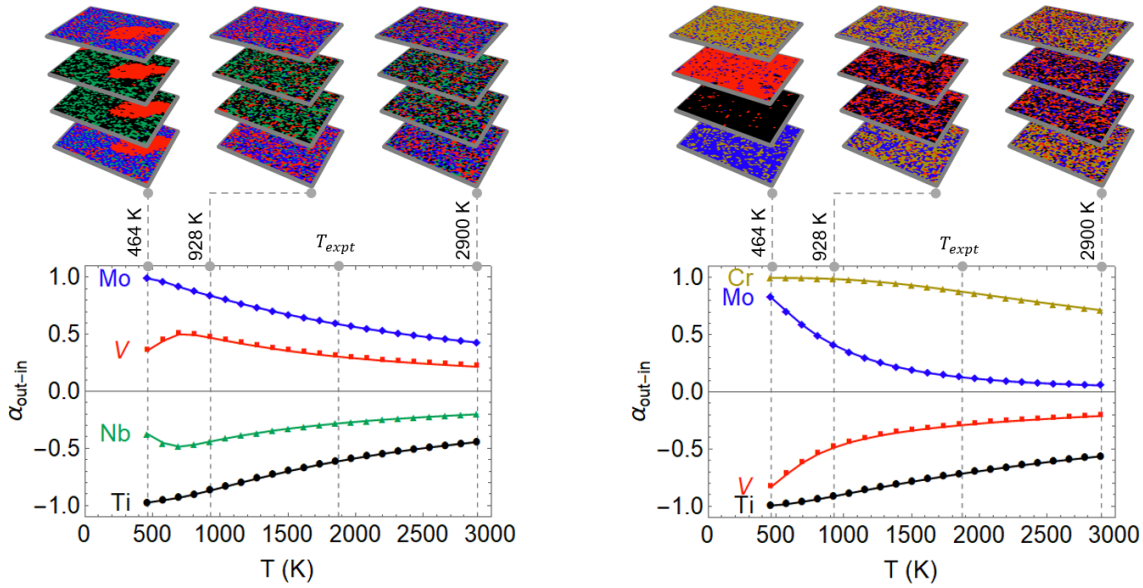

Figure 1. Structures of high-entropy (HE) MXenes (a) $TiVNbMoC_3$ and (b) $TiVCrMoC_3$ from first-principles-based Monte Carlo simulations. Top: Snapshots of the MXene atomic configurations at three representative temperatures, illustrating the complex interlayer and intralayer behaviors. (Carbon atoms are omitted for clarity.) For comparison, the experiment synthesis temperature, T_{expt}, is 1873K.[15] Bottom: The degree of interlayer segregation, $\alpha_{\text{out-in}}$, for each element with respect to temperature. A value of $+1$ (-1) corresponds to a complete segregation of the elemental species to the outer (inner) layers. Notably, Mo and Cr have the strongest tendency to be on the outer layers in (a) and (b), respectively.

Intralayer chemical order

Knowing that two of the four TMs tend to segregate to the outer layers and the other two to the inner layers, we next explore how the TM species coexist within each M layer. From the structures illustrated in Figure 1, we observe that the TM species in each M layer remain disordered (random SS) over a wide temperature range, from 928 K to 2900 K. As an advantage over earlier

computational works,[10] our Monte Carlo simulation results allow us to further characterize the atomic arrangements within each M layer of the HE M_4C_3 MXenes. We compute the chemical order within each M layer to quantify the level of intralayer pairwise clustering between the TM species using the Warren-Cowley short-range order (SRO) parameter.[32] For a given pair of TM elements, by definition, a zero, positive, and negative SRO indicates a random arrangement, separation tendency, and clustering tendency, respectively (see Methods section for details). We investigated the chemical order for the following pairs of elements: Ti-V, Ti-Nb, V-Nb, V-Mo, and Nb-Mo in $TiVNbMoC_3$ (Figure 2a) and Ti-V, Ti-Mo, V-Cr, V-Mo, and Cr-Mo in $TiVCrMoC_3$ (Figure 2b).

Figure 2 shows that at 2900 K (~1000 K above typical synthesis temperatures[15]), the TMs within each layer of $TiVNbMoC_3$ and $TiVCrMoC_3$ are largely randomly dispersed as solid solutions. As temperature decreases, we observe appreciable intralayer chemical order in $TiVNbMoC_3$ at moderate temperatures (~1000 K), where V and Nb tend to separate from each other in both the inner and outer M layers, while Mo and Nb tend to cluster together in the outer layers. Similarly, in $TiVCrMoC_3$ at ~1000 K, V tends to separate from Ti in the inner layers and from Mo in the M outer layers, while V and Cr tend to cluster together in the outer layers.

Below around 600 K, the intralayer atomic arrangements of both HE MXenes become more complex. Although annealing at such low temperatures may be infeasible in experiments, insights into the structures are nonetheless valuable for understanding the overall behavior of HE MXenes. For $TiVNbMoC_3$, the degree of intralayer chemical order increases at such low temperatures, with V separating from Nb and Ti in the inner layers and from Nb and Mo in the outer layers. This separation of V atoms leads to the formation of V-rich clusters in each M layer, as illustrated by the low-temperature structure in Figure 1a (at 464 K). Furthermore, the V-rich clusters in both

inner and outer layers tend to align across the four layers. This interlayer alignment of V clusters in the M layers competes against the interlayer segregation of V, which explains the weakening of the interlayer segregation of V and Nb below ~700 K seen in Figure 1a. The interlayer alignment of V-rich phases is most evident in DTM MXene $V_2Nb_2C_3$, as shown in the following section where we discuss HE MXenes similarities to DTM MXenes. Such interlayer alignments can, in principle, be characterized using an *interlayer* SRO, which could be relevant for future systematic studies of HE MXene structures at low temperatures (see Methods section for details).

For $TiVCrMoC_3$, Figure 2b shows that Ti separates from V and Mo in the inner M layers, while Mo separates from V and Cr in the outer layers below ~600K. However, as the low-temperature structure in Figure 1b illustrates, the lattice symmetry of $TiVCrMoC_3$ is spontaneously broken at low temperatures: although the two outer (inner) M layers in M_4C_3 MXene are symmetrically equivalent, all four M layers are now compositionally distinct with the TM species segregated across the four M^1-M^2-M^3-M^4 layers as Cr-V-Ti-Mo. As Figure 3 quantifies, the asymmetric interlayer segregation of atoms emerges sharply in $TiVCrMoC_3$ but is absent in $TiVNbMoC_3$ (see Methods section for the definition of the order parameter, α_{asym}). A similar asymmetry was previously predicted from first principles in DTM MXenes $(Ti\text{-}Nb)_3C_2$[33] and $TiMoCO_2$.[34] Similar to interlayer segregation, intralayer chemical order and asymmetric behavior will likely affect material properties and will be important considerations in MXene design.

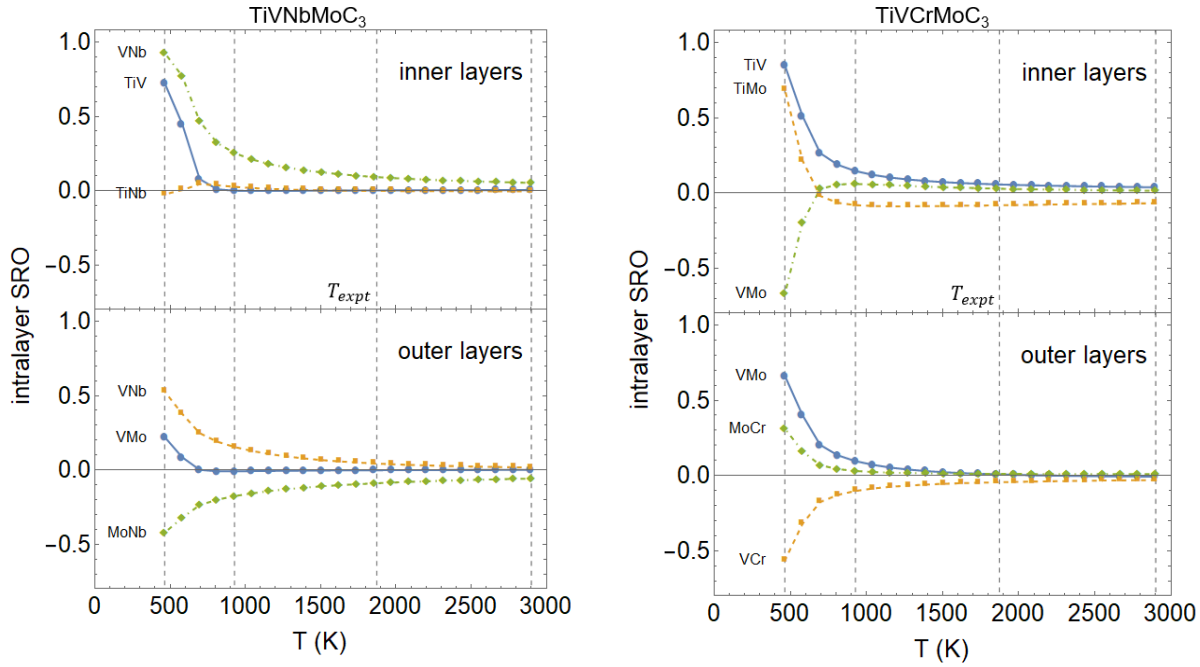

Figure 2. Intralayer chemical order of high-entropy MXenes (a) $TiVNbMoC_3$ and (b) $TiVCrMoC_3$ within the inner and outer layers, illustrating the separation (SRO > 0) and clustering (SRO < 0) tendencies between elemental pairs. Chemical orders involving elements with low content (*e.g.*, Ti in the outer layers) are not meaningful and have been omitted from the corresponding plots for clarity. The vertical dashed lines correspond to the representative temperatures in Figure 1.

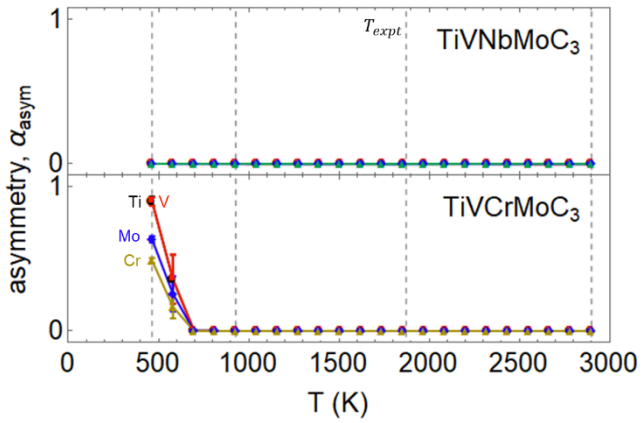

Figure 3. Asymmetric interlayer segregation of high-entropy MXenes (top) $TiVNbMoC_3$ and (bottom) $TiVCrMoC_3$ as temperature varies. For each elemental species, the order parameter, α_{asym}, quantifies the difference in concentration between the two inner M layers and

between the two outer M layers, with $\alpha_{\text{asym}} = 1(0)$ corresponding to a complete asymmetry (symmetry). The vertical dashed lines correspond to the representative temperatures in Figure 1.

Non-equicomposition

To elucidate compositional tuning of HE MXenes, we next study the MXene structures at non-equiatomic compositions. Following the experiments in Ref. [15], we vary the content of each TM species in turn, while keeping the remaining three species at equicomposition. Figure 4 shows that, across the 50 compositions studied, the relative tendencies of the TMs to occupy the outer/inner layers remain consistent. For example, Ti has the most negative $\alpha_{\text{out-in}}$ regardless of the composition, which means Ti prefers the inner M layers. However, the degree of interlayer segregation is composition dependent, particularly for V and Nb in $(Ti\text{-}V\text{-}Nb\text{-}Mo)_4C_3$ and Mo and V in $(Ti\text{-}V\text{-}Cr\text{-}Mo)_4C_3$. For example, Figure 4a shows that increasing the Ti content beyond the equimolar in $(Ti\text{-}V\text{-}Nb\text{-}Mo)_4C_3$ expels Nb and V from the inner layers, due to Ti having a stronger preference for the inner layers than Nb and V. Consequently, $\alpha_{\text{out-in}}$ increases for both Nb and V, and hence, interlayer segregation becomes weaker for Nb but stronger for V. Due to similar reasons, increasing the Nb content beyond the equimolar in $(Ti\text{-}V\text{-}Nb\text{-}Mo)_4C_3$ expels V (but not Ti) from the inner layers, leading to an increased interlayer segregation for V. Notably, at very low Ti content, V slightly favors the inner layers. This is because the outer layers can no longer accommodate all of Mo and V; hence, some V atoms (which has a weaker surface segregation tendency) spill over to the inner layers. Similarly, Figure 4b shows that increasing the Cr content in $(Ti\text{-}V\text{-}Cr\text{-}Mo)_4C_3$ expels Mo from the outer layers to the inner layers, due to Cr's stronger surface segregation tendency. The interlayer segregation for all other compositions in Figure 4 follows similar principles. Together, these results reinforce the observation about the species' preference for the outer layers: Cr > Mo > V > Nb > Ti. This holds true in the HE MXenes even

at non-equiatomic compositions. The strong variation of interlayer segregation highlights the tunability of HE MXenes.

As a note, the segregation of Cr is the least tunable because, compared with the other TM species, Cr has a much stronger preference for the outer layers. This suggests that, in HE MXene design, one can select combinations of TM species with the appropriate relative occupation tendencies to control the variability of interlayer segregation. Additionally, we note that in the experimental synthesis of HE MXenes,[15] any variations of TMs from equimolar led to the formation of impure phases, such as other types of MXene precursors (MAX phases) or binary carbides.

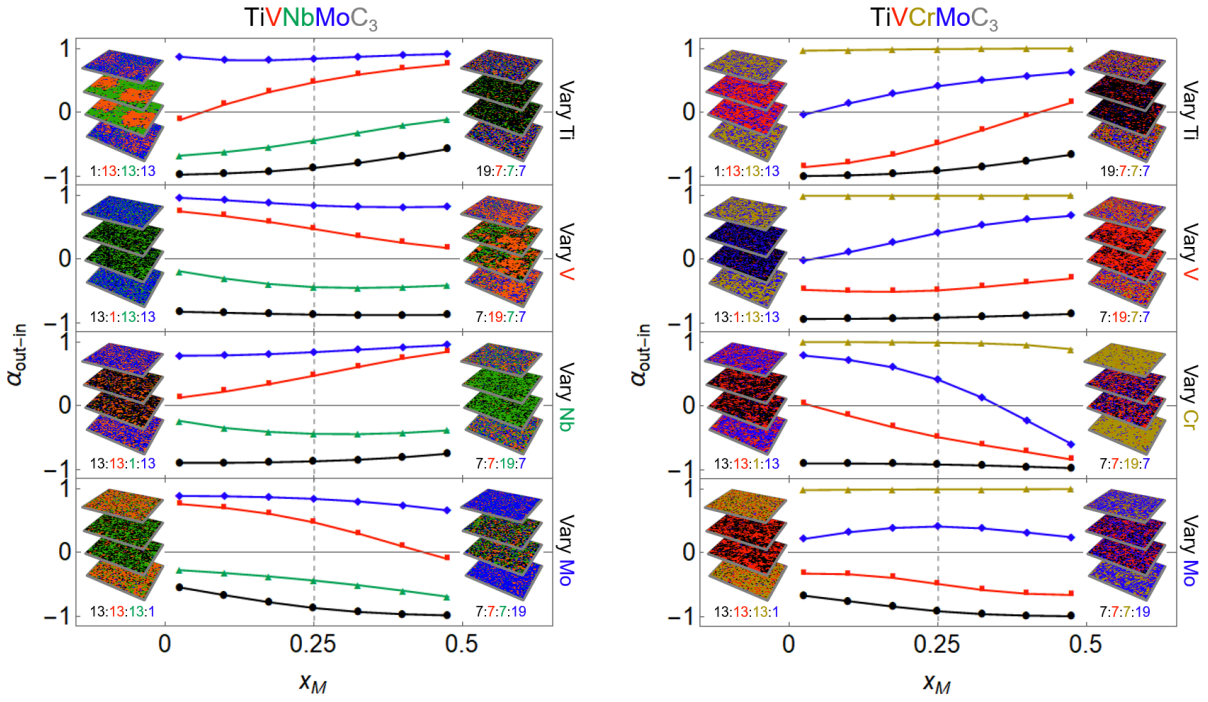

Figure 4. Compositional dependence of interlayer segregation, $\alpha_{\text{out-in}}$, in high-entropy MXenes (a) $(TiVNbMo)_4C_3$ and (b) $(TiVCrMo)_4C_3$ at 928 K. A value of $+1$ (-1) corresponds to complete segregation on the outer (inner) layers. The content of each elemental species M is varied in turn, while the remaining three species are fixed at equicomposition. The MXene structures on the left and right of each plot correspond to the end points, with the stoichiometric ratio Ti:V:Nb:Mo and Ti:V:Cr:Mo stated underneath the structures. The vertical dashed lines correspond to the MXenes at equimolar compositions.

Tracking the intralayer chemical order across the 50 compositions reinforces our earlier observations about V-Nb separation tendency in $(Ti\text{-}V\text{-}Nb\text{-}Mo)_4C_3$. Since single-phase MXenes may not be synthesizable at compositions with substantial intralayer separation, understanding how V-Nb separation (at moderate temperatures) can be suppressed is important for MXene design. Figure 5a shows that the separation is more pronounced at higher V content and lower Ti content, which is likely because the separation requires substantial amounts of V and Nb in the inner layers. This observation suggests that avoiding such regions in the compositional space would suppress V-Nb separation and hence may improve synthesizability.

In bulk HEAs, the increased configurational entropy due to the presence of more principal elements helps stabilize the SS phase.[21] Here, we demonstrate a similar behavior for HE MXenes. As Figure 5b shows, the predominant intralayer V-Nb separation is weaker in the HE MXene compared to its counterparts with fewer principal elements. The suppression of intralayer chemical order stabilizes the SS within each MXene layer, which suggests that HE MXenes with more principal TM elements (beyond four Ms) are generally more synthesizable. As a note, we do not observe any asymmetric interlayer segregation (where all four layers are compositionally distinct) among the non-equiatomic compositions at 928 K.

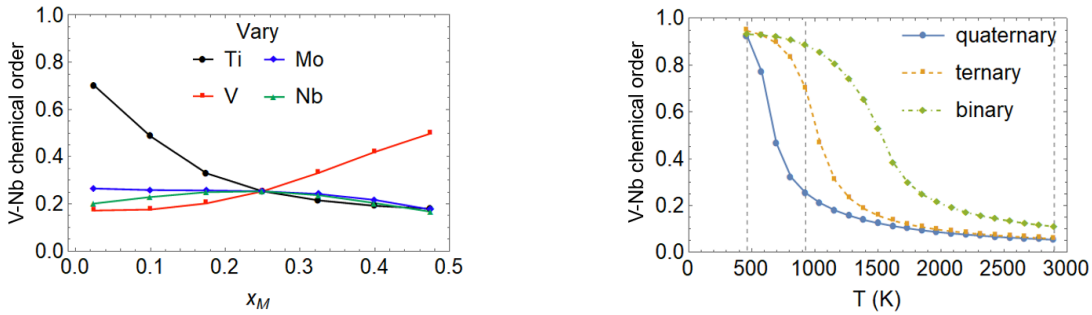

(a) (b)

Figure 5. Variation of the predominant V-Nb chemical order in the inner layers of $(Ti\text{-}V\text{-}Nb\text{-}Mo)_4C_3$ MXenes. A chemical order of +1 corresponds to a complete separation. (a) The

composition is varied as in Figure 4a at 928 K—the content of each elemental species M is varied in turn, while the remaining three species are fixed at equicomposition. The intersection at $x_M = 0.25$ corresponds to equicomposition. (b) The number of principal elements is varied. The MXene with two, three, and four principal elements corresponds to $V_2Nb_2C_3$, $Ti_{0.1}V_{1.3}Nb_{1.3}Mo_{1.3}C_3$, and $TiVNbMoC_3$, respectively. The vertical dashed lines correspond to the representative temperatures in Figure 1. We considered $Ti_{0.1}V_{1.3}Nb_{1.3}Mo_{1.3}C_3$ as a ternary principal elements MXene because it contains a trace amount of Ti. This phase is highlighted over the case without any Ti (*i.e.*, $V_{4/3}Nb_{4/3}Mo_{4/3}C_3$) because it corresponds to the structure illustrated in Figure 4a (top left).

Comparison with double-transition-metal (DTM) MXenes

Since HE MXenes were synthesized only recently,[15–19] there is a dearth of experimental data for direct comparison with our predicted atomic arrangements. Therefore, we look into the DTM MXenes to rationalize our findings. Existing experiments revealed that $Mo_2Ti_2C_3$, Mo_2TiC_2, Mo_2ScC_2, and Cr_2TiC_2 MXenes exhibit interlayer segregation with Mo and Cr occupying the outer layers.[8,10] First-principles computations also predicted interlayer segregation in $Mo_2V_2C_3$, $Mo_2Nb_2C_3$, $Cr_2Ti_2C_3$, $Cr_2V_2C_3$, $Cr_2Nb_2C_3$, $V_2Nb_2C_3$, $V_2Ti_2C_3$, and $Ti_2Nb_2C_3$,[10,33] where the first TM labelled in the formulae occupies the outer M layers. These observations from DTM MXenes imply a relative outer layer preference with Cr, Mo > V > Ti > Nb, which is consistent with the relative interlayer segregation tendencies we observe in the HE MXenes, except for the Ti-Nb pair.

To elucidate the structure of $Ti_2Nb_2C_3$, we show in Figure 6a our Monte Carlo results for this DTM MXene. In contrast to Ref. [10], which predicts Ti (Nb) preferring the outer (inner) layers, our results reveal that this DTM MXene has negligible interlayer segregation even at temperatures as low as 464 K; instead, it exhibits intralayer separation. We attribute this discrepancy to the omission of entropic effects in Ref. [10]; our Monte Carlo simulations correctly include the effects of configurational entropy and thoroughly sample the configurational space to determine the thermodynamic equilibrium structure. For similar reasons, our results for $V_2Nb_2C_3$ in Figure 6b

reveal intralayer separation in addition to just the interlayer segregation predicted in Ref. [10]. For the remaining DTM MXenes in Figure 6b, our results and Ref. [10] are consistent.

Notably, the nine DTM MXenes in Figure 6b exhibit structures with various degrees of interlayer segregation, from the strongly segregated $Mo_2Ti_2C_3$ to the non-segregated $Nb_2Ti_2C_3$. (See Figure S1 for a full characterization of the DTM MXenes.) Comparing these with the interlayer segregation in HE MXenes reveals no evidence that the increased number of principal TM elements in HE MXenes helps suppress interlayer segregation. This starkly contrasts the case for intralayer chemical order: as demonstrated in the preceding section, intralayer chemical order is weaker in HE MXenes. The contrast arises because interlayer segregation, unlike intralayer chemical order, is largely a non-interacting effect, in which each M layer is occupied based on the single-site energies of each TM species; this is supported by Figure 8a illustrating that the single-site energies in the surrogate models dominate the multi-site interactions. Consequently, the suppression of interlayer segregation due to configurational entropy does not apply to intralayer chemical order.

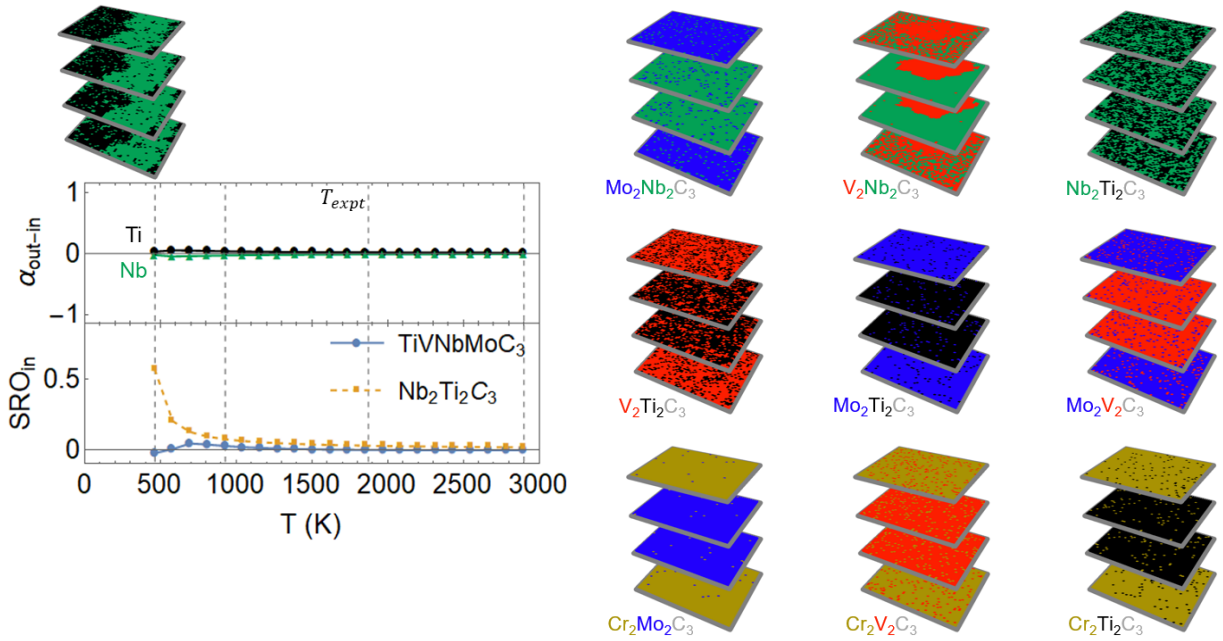

(a) (b)

Figure 6. (a) The structure of $Nb_2Ti_2C_3$ at 464 K, illustrating intralayer separation (SRO $>$ 0) without interlayer segregation ($\alpha_{\text{out-in}} \approx 0$) at low temperatures. For comparison, the Nb-Ti SRO in the inner layers of $TiVNbMoC_3$ is included in the same plot, where a value of 0 corresponds to a random atomic arrangement. The vertical dashed lines correspond to the representative temperatures in Figure 1. (b) The structures of the nine constituent double-transition-metal (DTM) MXenes of the high-entropy MXenes $TiVNbMoC_3$ and $TiVCrMoC_3$ at 928 K. For ease of comparison, species with a stronger preference for the outer layers in the high-entropy MXenes are written first in the chemical formulae (*i.e.*, Cr > Mo > V > Nb > Ti).

Deducing the structures of HE MAX phases and surface-terminated MXenes

Although our results are based on bare MXenes, we speculate that the atomic configurations elucidated here are also representative of surface-terminated MXenes obtained after etching the parent MAX phases in experiments. Because the low temperature (328 K[15]) at which the MAX phases are etched precludes any significant atomic rearrangements, the atomic configurations of TM elements in the MAX phase precursors would remain largely the same after etching. Therefore,

it suffices to computationally demonstrate that similar atomic configurations of the TM elements are observed in the bare MXenes and the parent MAX phases.

We focus on the predominant behavior, *i.e.*, interlayer segregation. Based on a small set of first-principles data, we construct a minimal cluster expansion (CE) for each of the HE MXenes $TiVNbMoC_3$ and $TiVCrMoC_3$, as well as the parent MAX phases $TiVNbMoAlC_3$ and $TiVCrMoAlC_3$ (see Methods section for details). The single-site energies in the minimal CEs indicate the relative tendency of each TM species to occupy the outer layers. As Figure 7 shows, the tendencies are similar in both the MXene and the MAX phase: (a) Mo > V > Nb > Ti in $TiVNbMoC_3$ and $TiVNbMoAlC_3$, and (b) Cr > Mo > V > Ti in $TiVCrMoC_3$ and $TiVCrMoAlC_3$. These results indicate that Mo and V (Ti and Nb) tend to segregate to the outer (inner) layers of $TiVNbMoC_3$ and $TiVNbMoAlC_3$, while Cr and Mo (Ti and V) tend to segregate to the outer (inner) layers of $TiVCrMoC_3$ and $TiVCrMoAlC_3$. Therefore, the interlayer segregation we reported in the bare HE MXenes is largely independent of terminations—it also occurs in the MAX phases, as well as in terminated HE MXenes.

Nevertheless, we note that the single-site energies shown in Figure 7a are consistently higher in $TiVNbMoAlC_3$ than in $TiVNbMoC_3$. This suggests that, compared with the bare $TiVNbMoC_3$ MXene, interlayer segregation will be more prominent in the parent MAX phase and hence in the derived terminated $TiVNbMoC_3$.

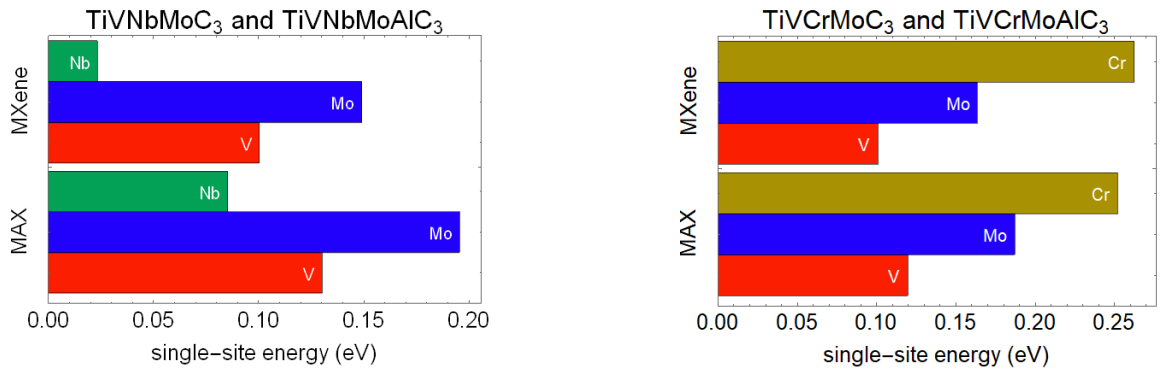

(a) (b)

Figure 7. The single-site energies in a minimal cluster expansion of high-entropy MXenes (a) $TiVNbMoC_3$ and (b) $TiVCrMoC_3$, compared with those for the corresponding MAX phases. These energies correspond to the tendency of the transition-metal species to occupy the outer layers. The energies are defined relative to Ti, so the single-site energies for Ti are zero by definition.

Conclusion

To conclude, using Monte Carlo simulations based on effective interactions derived from first-principles data, we have elucidated the complex atomic arrangements in high-entropy (HE) MXenes $TiVNbMoC_3$ and $TiVCrMoC_3$. Consistently across the compositions studied, both HE MXenes exhibit significant preferential occupancy of the transition metals (TMs) in the four M layers in MXenes as interlayer segregation even at temperatures as high as 2900 K. In general, the outer (inner) layers are predominantly occupied by two of the four TM species interspersed with a third minority species. Specifically, Cr most strongly prefers the outer layers, followed by Mo, V, Nb, and Ti. The degree of interlayer segregation strongly depends on the composition, highlighting the tunability of HE MXenes.

Furthermore, each M layer in M_4C_3 is largely a random solid solution at the synthesis temperature of MXenes precursors (> 1873 K). However, our calculations indicate that at lower

temperatures (below 928 K), a notable tendency for Nb and V atoms to separate from each other within the inner layers was observed. This Nb-V chemical order is most prominent at low Ti and high V contents, and compared with the double-transition-metal (DTM) MXenes, the intralayer chemical order is suppressed in HE MXenes due to the increased configurational entropy. The intralayer chemical order might not be easily achieved in synthesized MXenes because of the sluggish diffusion kinetics of TMs at low temperatures. With HE MXenes only recently synthesized,[15] these insights into the MXene structures will accelerate the development of design principles for HE MXenes to help efficiently navigate the huge compositional space towards candidates with desired properties.

Computational methods

DFT calculations

The energies of the CE training structures are calculated based on density functional theory (DFT) with the Vienna Ab initio Simulation Package (VASP).[35,36] We use the Perdew, Burke, and Ernzerhof (PBE) exchange correlation based on the generalized gradient approximation (GGA).[37,38] The projector augmented-wave (PAW) potentials are used with the outer p semicore states included in the valence states.[39,40] Planewave cutoffs are set to 500 eV. Our convergence criterion is based on keeping the Hellmann-Feynman force on each atom below 0.01 eV/Å. Calculations are spin polarized with ISPIN set to 2. The initial magnetic moment of each atom is set to 1, representative of the ferromagnetic state. The k-point mesh is generated using a Γ grid and density of 200 $Å^{-3}$. To minimize spurious interactions between periodic images, a vacuum of at least 15 Å along the z-direction is ensured.

Cluster expansion

Our cluster expansion (CE) formalism follows our previous works.[29,30] Based on the generalized Ising model, CE expands the configurational energy $E(\sigma)$ of an alloy structure, σ, in terms of atomic clusters α, where the cluster correlation functions $\Phi_\alpha(\sigma)$ serve as the basis set and the effective cluster interactions (ECIs) V_α serve as the coefficients: $E(\sigma) = \sum_\alpha \Phi_\alpha(\sigma) V_\alpha$.

The CE for each of the two HE MXenes is trained with the formation energies of 795 MXene structures from DFT. The training structures are randomly selected from the pool of derivative structures with up to a (8×7)-atom unit cell.[41,42] Containing between two to four TM species, the structures span a large compositional space.

For an N-component system, since the concentrations of the N species sum to one, only $N - 1$ of the N concentrations are independent variables, while the remaining one is a dependent variable. Therefore, there are always $N - 1$ independent species and one dependent species. In our CE, we treat V, Mo, Nb, and Cr as the independent species, while Ti is treated as dependent. As such, only clusters formed by V, Mo, Nb, and Cr atoms are required. In the MXene lattice, we consider one set of singlets, up to the 8th-nearest-neighbor (8NN) pairs, 10NN triplets, and 3NN quadruplets. These correspond to an initial pool of 328 symmetrically distinct clusters, consisting of 3 singlets, 60 pairs, 175 triplets, and 90 quadruplets. Figure 8b illustrates five examples of these clusters. Each singlet is defined to be the single-site energy of an element on the inner layers relative to the outer layers, such that a positive (negative) singlet ECI indicates the element's preference for the outer (inner) layers.

Our fitting procedure follows our earlier work in Ref. 30. Using the DFT formation energies of the training structures, we use *group lasso*, a machine learning technique, to select a properly truncated CE set from the initial 328 distinct clusters. Fivefold cross-validation (CV) is used for selecting the optimal hyperparameter with the one-standard-error rule. Figure 8 shows that, in the

trained CEs for $(Ti\text{-}V\text{-}Nb\text{-}Mo)_4C_3$ and $(Ti\text{-}V\text{-}Cr\text{-}Mo)_4C_3$, 170 and 234 out of the initial 328 clusters are selected with a CV score of 5.8 meV and 5.0 meV, respectively. The fitted ECIs exhibit good convergence—the magnitude of the ECIs generally decreases with increasing cluster size. The singlet ECIs for the various elemental species satisfy the following: $0 < Nb < V < Mo \ll Cr$, which is consistent with the MXenes' interlayer segregation tendency illustrated in Figure 1 and Figure 4. Notably, the relatively large singlet ECI for Cr indicates that it is much more energetically favorable for Cr atoms to occupy the outer layers than the inner layers.

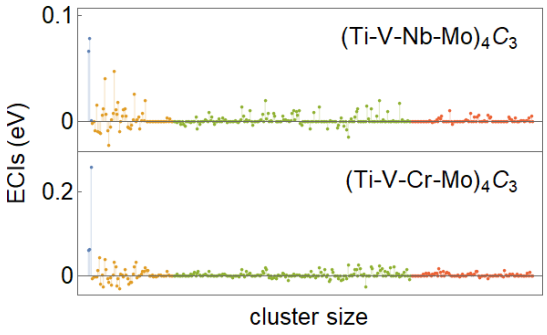

(a)

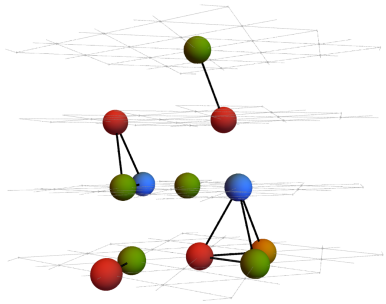

(b)

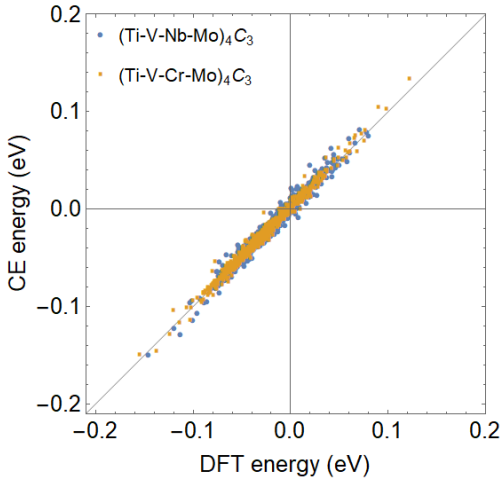

(c)

Figure 8. Cluster expansions (CE) of high-entropy MXenes $(Ti\text{-}V\text{-}Nb\text{-}Mo)_4C_3$ and $(Ti\text{-}V\text{-}Cr\text{-}Mo)_4C_3$, with cross validation scores of 5.8 meV and 5.0 meV, respectively. Each CE is trained with the first-principles formation energies of 795 MXene structures. (a) The fitted values of the 328 ECIs in each of the CEs. Singlets, pairs, triplets, and quadruplets are colored blue, orange, green, and red, respectively. (b) Five examples of the clusters used: a singlet, an intralayer pair, an interlayer pair, a triplet, and a quadruplet. (c) A plot of the predicted CE energies against the DFT energies for the training structures.

Minimal cluster expansion

The minimal cluster expansions (CEs) used to discuss the effects of surface terminations follow the formalism detailed in the preceding subsection but consist only of one set of singlets, *i.e.*, without any pairs, triplets, etc. Using the least squares method, each CE is fitted with the DFT formation energies of twelve equicompositional structures with the smallest unit cells (*i.e.*, one atom per layer). These structures form a minimal set that captures the various types of interlayer segregation, *e.g.*, with the four M^1-M^2-M^3-M^4 layers as Ti-Mo-V-Nb or Ti-Mo-Nb-V, etc. For some of these structures, the dashed grey lines in Figure 9 indicate significant energy differences between the MXenes and the MAX phases. Nevertheless, as Figure 9 shows, the CE fits for both phases appear reasonably good despite the minimal models.

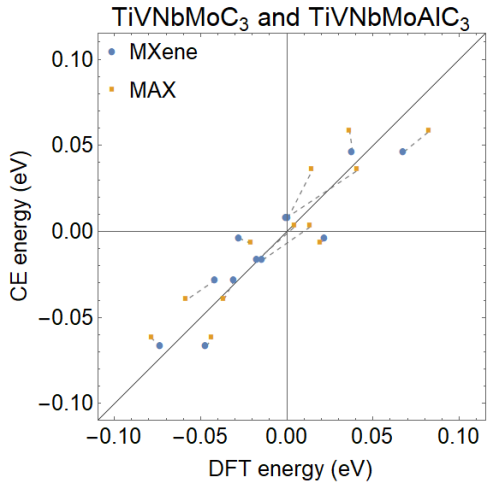

(a)

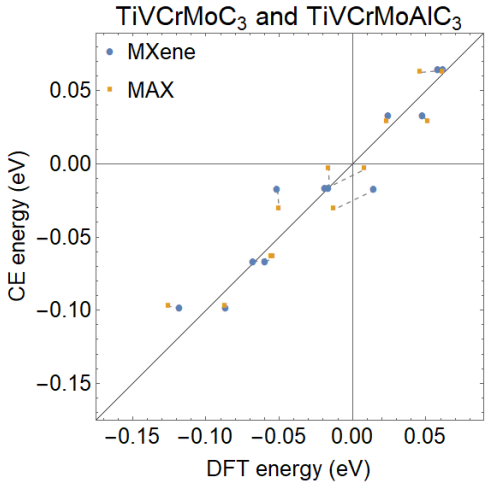

(b)

Figure 9. Plots of the energies given by the minimal cluster expansion (CE) models against the DFT energies for the twelve training structures for (a) $TiVNbMoC_3$ and $TiVNbMoAlC_3$, and (b) $TiVCrMoC_3$ and $TiVCrMoAlC_3$. In each plot, the dashed grey lines connect each MXene structure with the same structure in the MAX phase, indicating the change in energy between the two phases.

Monte Carlo (MC) simulations

Our canonical MC simulations are based on the Metropolis algorithm as implemented in our Thermodynamic Toolkit (TTK).[43,44] Each simulation contains $48 \times 48 \times 4$ atoms within the periodic simulation box, using 1000 equilibrium steps and 10000 sampling steps. At each composition, the simulation begins in the solid solution phase at a high temperature of 2900 K and cools with a temperature step of $\Delta T \approx 116$ K, for a total of 22 temperatures.

Statistical errors are computed for Figure 1, Figure 2, and Figure 3 by repeating the MC simulations with 20 different random seeds. The error bars for these figures are too small to be visible, except for Figure 3 (bottom).

Short-range order (SRO) parameters

The intralayer chemical order is characterized using the Warren-Cowley short-range order (SRO) parameters to track the elemental distributions. In our work, we focus on the nearest-neighbor (NN) SRO parameter. For elemental species $i \neq j$, the NN SRO parameter is given by $\alpha_{ij} = 1 - p_{ij}/c_i c_j$, where c_i, c_j are the concentrations of species i, j, and p_{ij} is the probability of a NN atomic pair having species i, j in the first and second sites, respectively. It follows that $\alpha = 0$ indicates a fully random arrangement, $0 < \alpha \leq 1$ a separation tendency, and $\alpha < 0$ a tendency for the species to cluster.

In principle, an analogous interlayer SRO can also be defined to characterize any interlayer chemical order by tracking atomic pairs that span different layers. *E.g.*, the alignment of V-rich

clusters across different M layers in Figure 1a would correspond to a positive interlayer SRO for V-Mo, V-Nb, and V-Ti elemental pairs. However, such a characterization is beyond the scope of the present work. This is because tracking SRO in general incurs computational overheads during Monte Carlo simulations. Judging that the distance between TM layers is large and separated by carbon layer, we expect interlayer interactions in general to be weaker. Hence, we reserve the tracking of SRO only to short interatomic distances within the layer (intralayer).

Asymmetry order parameters

We characterize the asymmetry in HE MXenes, where the two inner (outer) layers become compositionally distinct, using the order parameter:

$$\alpha_{\mathrm{asym}} = \frac{|\delta x_M^{\mathrm{out}}| + |\delta x_M^{\mathrm{in}}|}{x_M^{\mathrm{tot}}}, \tag{2}$$

where $\delta x_M^{\mathrm{out(in)}}$ is the difference in the concentration of species M between the two outer (inner) layers, while x_M^{tot} is the total concentration across all four layers. By definition, $\alpha_{\mathrm{asym}} = 1(0)$ corresponds to a complete asymmetry (symmetry).

ASSOCIATED CONTENT

Supporting Information

Characterization of the nine constituent DTM MXenes of the high-entropy MXenes $TiVNbMoC_3$ and $TiVCrMoC_3$. (PDF)

AUTHOR INFORMATION

Corresponding Author

* E-mail: tantl@ihpc.a-star.edu.sg

Author Contributions

The manuscript was written through contributions of all authors. All authors have given approval to the final version of the manuscript.

ACKNOWLEDGMENT

This work is supported by the Advanced Manufacturing and Engineering Young Individual Research Grant (AME YIRG) of Agency for Science, Technology and Research (A∗STAR) (A1884c0016). H.J. acknowledges support from the Structural Metal Alloys Programme of Agency for Science, Technology and Research (A*STAR) (A18B1b0061). The authors acknowledge the use of high-performance computing resources in the National Supercomputing Centre, Singapore (https://www.nscc.sg) and the A*STAR Computational Resource Centre (ACRC) in Singapore for the DFT and Monte Carlo computations, respectively. K.N. and B.A. acknowledge the funding support from the U.S. National Science Foundation under Grant No. DMR-2124478.

REFERENCES

(1) Naguib, M.; Kurtoglu, M.; Presser, V.; Lu, J.; Niu, J.; Heon, M.; Hultman, L.; Gogotsi, Y.; Barsoum, M. W. Two-Dimensional Nanocrystals Produced by Exfoliation of Ti3AlC2. *Adv. Mater.* **2011**, *23* (37), 4248–4253. https://doi.org/10.1002/adma.201102306.

(2) Anasori, B.; Lukatskaya, M. R.; Gogotsi, Y. 2D Metal Carbides and Nitrides (MXenes) for Energy Storage. *Nat. Rev. Mater.* **2017**, *2* (2), 1–17. https://doi.org/10.1038/natrevmats.2016.98.

(3) Gogotsi, Y.; Anasori, B. The Rise of MXenes. *ACS Nano* **2019**, *13* (8), 8491–8494. https://doi.org/10.1021/acsnano.9b06394.

(4) Naguib, M.; Barsoum, M. W.; Gogotsi, Y. Ten Years of Progress in the Synthesis and Development of MXenes. *Adv. Mater.* **2021**, *33* (39), 2103393. https://doi.org/10.1002/adma.202103393.

(5) VahidMohammadi, A.; Rosen, J.; Gogotsi, Y. The World of Two-Dimensional Carbides and Nitrides (MXenes). *Science* **2021**, *372* (6547), eabf1581. https://doi.org/10.1126/science.abf1581.

(6) Gao, L.; Li, C.; Huang, W.; Mei, S.; Lin, H.; Ou, Q.; Zhang, Y.; Guo, J.; Zhang, F.; Xu, S.; Zhang, H. MXene/Polymer Membranes: Synthesis, Properties, and Emerging Applications. *Chem. Mater.* **2020**, *32* (5), 1703–1747. https://doi.org/10.1021/acs.chemmater.9b04408.

(7) Ahmed, A.; Hossain, M. M.; Adak, B.; Mukhopadhyay, S. Recent Advances in 2D MXene Integrated Smart-Textile Interfaces for Multifunctional Applications. *Chem. Mater.* **2020**, *32* (24), 10296–10320. https://doi.org/10.1021/acs.chemmater.0c03392.
(8) Meshkian, R.; Tao, Q.; Dahlqvist, M.; Lu, J.; Hultman, L.; Rosen, J. Theoretical Stability and Materials Synthesis of a Chemically Ordered MAX Phase, Mo2ScAlC2, and Its Two-Dimensional Derivate Mo2ScC2 MXene. *Acta Mater.* **2017**, *125*, 476–480. https://doi.org/10.1016/j.actamat.2016.12.008.
(9) Persson, I.; el Ghazaly, A.; Tao, Q.; Halim, J.; Kota, S.; Darakchieva, V.; Palisaitis, J.; Barsoum, M. W.; Rosen, J.; Persson, P. O. Å. Tailoring Structure, Composition, and Energy Storage Properties of MXenes from Selective Etching of In-Plane, Chemically Ordered MAX Phases. *Small* **2018**, *14* (17), 1703676. https://doi.org/10.1002/smll.201703676.
(10) Anasori, B.; Xie, Y.; Beidaghi, M.; Lu, J.; Hosler, B. C.; Hultman, L.; Kent, P. R. C.; Gogotsi, Y.; Barsoum, M. W. Two-Dimensional, Ordered, Double Transition Metals Carbides (MXenes). *ACS Nano* **2015**, *9* (10), 9507–9516. https://doi.org/10.1021/acsnano.5b03591.
(11) Wong, Z. M.; Tan, T. L.; Tieu, A. J. K.; Yang, S.-W.; Xu, G. Q. Computational Discovery of Transparent Conducting In-Plane Ordered MXene (i-MXene) Alloys. *Chem. Mater.* **2019**, *31* (11), 4124–4132. https://doi.org/10.1021/acs.chemmater.9b00881.
(12) Dahlqvist, M.; Rosen, J. Predictive Theoretical Screening of Phase Stability for Chemical Order and Disorder in Quaternary 312 and 413 MAX Phases. *Nanoscale* **2020**, *12* (2), 785–794. https://doi.org/10.1039/C9NR08675G.
(13) Hong, W.; Wyatt, B. C.; Nemani, S. K.; Anasori, B. Double Transition-Metal MXenes: Atomistic Design of Two-Dimensional Carbides and Nitrides. *MRS Bull.* **2020**, *45* (10), 850–861. https://doi.org/10.1557/mrs.2020.251.
(14) Gogotsi, Y.; Huang, Q. MXenes: Two-Dimensional Building Blocks for Future Materials and Devices. *ACS Nano* **2021**, *15* (4), 5775–5780. https://doi.org/10.1021/acsnano.1c03161.
(15) Nemani, S. K.; Zhang, B.; Wyatt, B. C.; Hood, Z. D.; Manna, S.; Khaledialidusti, R.; Hong, W.; Sternberg, M. G.; Sankaranarayanan, S. K. R. S.; Anasori, B. High-Entropy 2D Carbide MXenes: TiVNbMoC3 and TiVCrMoC3. *ACS Nano* **2021**. https://doi.org/10.1021/acsnano.1c02775.
(16) Du, Z.; Wu, C.; Chen, Y.; Cao, Z.; Hu, R.; Zhang, Y.; Gu, J.; Cui, Y.; Chen, H.; Shi, Y.; Shang, J.; Li, B.; Yang, S. High-Entropy Atomic Layers of Transition-Metal Carbides (MXenes). *Adv. Mater.* **2021**, *33* (39), 2101473. https://doi.org/10.1002/adma.202101473.
(17) Du, Z.; Wu, C.; Chen, Y.; Zhu, Q.; Cui, Y.; Wang, H.; Zhang, Y.; Chen, X.; Shang, J.; Li, B.; Chen, W.; Liu, C.; Yang, S. High-Entropy Carbonitride MAX Phases and Their Derivative MXenes. *Adv. Energy Mater.* **2022**, *12* (6), 2103228. https://doi.org/10.1002/aenm.202103228.
(18) Zhou, J.; Tao, Q.; Ahmed, B.; Palisaitis, J.; Persson, I.; Halim, J.; Barsoum, M. W.; Persson, P. O. Å.; Rosen, J. High-Entropy Laminate Metal Carbide (MAX Phase) and Its Two-Dimensional Derivative MXene. *Chem. Mater.* **2022**, *34* (5), 2098–2106. https://doi.org/10.1021/acs.chemmater.1c03348.
(19) Etman, A. S.; Zhou, J.; Rosen, J. Ti1.1V0.7Cr Nb1.0Ta0.6C3T High-Entropy MXene Freestanding Films for Charge Storage Applications. *Electrochem. Commun.* **2022**, *137*, 107264. https://doi.org/10.1016/j.elecom.2022.107264.
(20) Yeh, J. W.; Chen, Y. L.; Lin, S. J.; Chen, S. K. High-Entropy Alloys – A New Era of Exploitation. *Mater. Sci. Forum* **2007**, *560*, 1–9. https://doi.org/10.4028/www.scientific.net/MSF.560.1.

(21) George, E. P.; Raabe, D.; Ritchie, R. O. High-Entropy Alloys. *Nat. Rev. Mater.* **2019**, *4* (8), 515–534. https://doi.org/10.1038/s41578-019-0121-4.
(22) Sarker, P.; Harrington, T.; Toher, C.; Oses, C.; Samiee, M.; Maria, J.-P.; Brenner, D. W.; Vecchio, K. S.; Curtarolo, S. High-Entropy High-Hardness Metal Carbides Discovered by Entropy Descriptors. *Nat. Commun.* **2018**, *9* (1), 4980. https://doi.org/10.1038/s41467-018-07160-7.
(23) Castle, E.; Csanádi, T.; Grasso, S.; Dusza, J.; Reece, M. Processing and Properties of High-Entropy Ultra-High Temperature Carbides. *Sci. Rep.* **2018**, *8* (1), 8609. https://doi.org/10.1038/s41598-018-26827-1.
(24) Oses, C.; Toher, C.; Curtarolo, S. High-Entropy Ceramics. *Nat. Rev. Mater.* **2020**, *5* (4), 295–309. https://doi.org/10.1038/s41578-019-0170-8.
(25) Miracle, D. B.; Senkov, O. N. A Critical Review of High Entropy Alloys and Related Concepts. *Acta Mater.* **2017**, *122*, 448–511. https://doi.org/10.1016/j.actamat.2016.08.081.
(26) Zeng, Y.; Man, M.; Bai, K.; Zhang, Y.-W. Revealing High-Fidelity Phase Selection Rules for High Entropy Alloys: A Combined CALPHAD and Machine Learning Study. *Mater. Des.* **2021**, *202*, 109532. https://doi.org/10.1016/j.matdes.2021.109532.
(27) Li, J.-H.; Tsai, M.-H. Theories for Predicting Simple Solid Solution High-Entropy Alloys: Classification, Accuracy, and Important Factors Impacting Accuracy. *Scr. Mater.* **2020**, *188*, 80–87. https://doi.org/10.1016/j.scriptamat.2020.06.064.
(28) Sanchez, J. M.; Ducastelle, F.; Gratias, D. Generalized Cluster Description of Multicomponent Systems. *Phys. Stat. Mech. Its Appl.* **1984**, *128* (1–2), 334–350. https://doi.org/10.1016/0378-4371(84)90096-7.
(29) Leong, Z.; Ramamurty, U.; Tan, T. L. Microstructural and Compositional Design Principles for Mo-V-Nb-Ti-Zr Multi-Principal Element Alloys: A High-Throughput First-Principles Study. *Acta Mater.* **2021**, *213*, 116958. https://doi.org/10.1016/j.actamat.2021.116958.
(30) Leong, Z.; Tan, T. L. Robust Cluster Expansion of Multicomponent Systems Using Structured Sparsity. *Phys. Rev. B* **2019**, *100* (13), 134108. https://doi.org/10.1103/PhysRevB.100.134108.
(31) Sang, X.; Xie, Y.; Lin, M.-W.; Alhabeb, M.; Van Aken, K. L.; Gogotsi, Y.; Kent, P. R. C.; Xiao, K.; Unocic, R. R. Atomic Defects in Monolayer Titanium Carbide (Ti3C2Tx) MXene. *ACS Nano* **2016**, *10* (10), 9193–9200. https://doi.org/10.1021/acsnano.6b05240.
(32) Fontaine, D. D. The Number of Independent Pair-correlation Functions in Multicomponent Systems. *J. Appl. Crystallogr.* **1971**, *4* (1), 15–19. https://doi.org/10.1107/S0021889871006174.
(33) Tan, T. L.; Jin, H. M.; Sullivan, M. B.; Anasori, B.; Gogotsi, Y. High-Throughput Survey of Ordering Configurations in MXene Alloys Across Compositions and Temperatures. *ACS Nano* **2017**, *11* (5), 4407–4418. https://doi.org/10.1021/acsnano.6b08227.
(34) Wong, Z. M.; Deng, T.; Shi, W.; Wu, G.; Tan, T. L.; Yang, S.-W. High Performance Photocatalytic and Thermoelectric Two-Dimensional Asymmetrically Ordered Janus-like MXene Alloys. *Mater. Adv.* **2020**, *1* (5), 1176–1185. https://doi.org/10.1039/D0MA00391C.
(35) Kresse, G.; Furthmüller, J. Efficiency of Ab-Initio Total Energy Calculations for Metals and Semiconductors Using a Plane-Wave Basis Set. *Comput. Mater. Sci.* **1996**, *6* (1), 15–50. https://doi.org/10.1016/0927-0256(96)00008-0.
(36) Kresse, G.; Furthmüller, J. Efficient Iterative Schemes for Ab Initio Total-Energy Calculations Using a Plane-Wave Basis Set. *Phys. Rev. B* **1996**, *54* (16), 11169–11186. https://doi.org/10.1103/PhysRevB.54.11169.

(37) Perdew, J. P.; Burke, K.; Ernzerhof, M. Generalized Gradient Approximation Made Simple. *Phys. Rev. Lett.* **1996**, *77* (18), 3865–3868. https://doi.org/10.1103/PhysRevLett.77.3865.
(38) Perdew, J. P.; Burke, K.; Ernzerhof, M. Generalized Gradient Approximation Made Simple [Phys. Rev. Lett. 77, 3865 (1996)]. *Phys. Rev. Lett.* **1997**, *78* (7), 1396–1396. https://doi.org/10.1103/PhysRevLett.78.1396.
(39) Blöchl, P. E. Projector Augmented-Wave Method. *Phys. Rev. B* **1994**, *50* (24), 17953–17979. https://doi.org/10.1103/PhysRevB.50.17953.
(40) Kresse, G.; Joubert, D. From Ultrasoft Pseudopotentials to the Projector Augmented-Wave Method. *Phys. Rev. B* **1999**, *59* (3), 1758–1775. https://doi.org/10.1103/PhysRevB.59.1758.
(41) Hart, G. L. W. Out of the Scalar Sand Box. *Nat. Mater.* **2008**, *7* (6), 426–427. https://doi.org/10.1038/nmat2190.
(42) Hart, G. L. W.; Nelson, L. J.; Forcade, R. W. Generating Derivative Structures at a Fixed Concentration. *Comput. Mater. Sci.* **2012**, *59*, 101–107. https://doi.org/10.1016/j.commatsci.2012.02.015.
(43) Zarkevich, N. A.; Tan, T. L.; Johnson, D. D. First-Principles Prediction of Phase-Segregating Alloy Phase Diagrams and a Rapid Design Estimate of Their Transition Temperatures. *Phys. Rev. B* **2007**, *75* (10), 104203. https://doi.org/10.1103/PhysRevB.75.104203.
(44) Zarkevich, N. A.; Tan, T. L.; Wang, L.-L.; Johnson, D. D. Low-Energy Antiphase Boundaries, Degenerate Superstructures, and Phase Stability in Frustrated Fcc Ising Model and Ag-Au Alloys. *Phys. Rev. B* **2008**, *77* (14). https://doi.org/10.1103/PhysRevB.77.144208.

For Table of Contents Only